

Let it shine: Autofluorescence of Papanicolaou-stain improves AI-based cytological oral cancer detection

Wenyi Lian^a, Joakim Lindblad^a, Christina Runow Stark^{b,c}, Jan-Michaél Hirsch^b and Nataša Sladoje^{a,*}

^aCentre for Image Analysis, Department of Information Technology, Uppsala University, Uppsala, Sweden

^bDepartment of Surgical Sciences, Uppsala University, Uppsala, Sweden

^cFolkhelsevården, Region Uppsala, Uppsala, Sweden

ARTICLE INFO

Keywords:

Biomedical imaging
Multimodal microscopy
Deep learning
Multimodal information fusion
Artificial intelligence
Cytopathology

ABSTRACT

Background and objectives: Oral cancer is a global health challenge. The disease can be successfully treated if detected early, but the survival rate drops significantly for late stage cases. There is a growing interest in a shift from the current standard of invasive and time-consuming tissue sampling and histological examination, toward non-invasive brush biopsies and cytological examination, facilitating continued risk group monitoring. For cost effective and accurate cytological analysis, there is a great need for reliable computer-assisted data-driven approaches. However, infeasibility of accurate cell-level annotation hinders model performance, and limits evaluation and interpretation of the results. This study aims to improve AI-based oral cancer detection by introducing additional information through multimodal imaging and deep multimodal information fusion.

Methods: We combine brightfield and fluorescence whole slide microscopy imaging to analyze Papanicolaou-stained liquid-based cytology slides of brush biopsies collected from both healthy and cancer patients. Given the challenge of detailed cytological annotations, we utilize a weakly supervised deep learning approach only relying on patient-level labels. We evaluate various multimodal information fusion strategies, including early, late, and three recent intermediate fusion methods.

Results: Our experiments demonstrate that: (i) there is substantial diagnostic information to gain from fluorescence imaging of Papanicolaou-stained cytological samples, (ii) multimodal information fusion improves classification performance and cancer detection accuracy, compared to single-modality approaches. Intermediate fusion emerges as the leading method among the studied approaches. Specifically, the Co-Attention Fusion Network (CAFNet) model achieves impressive results, with an F1 score of 83.34% and an accuracy of 91.79% at cell level, surpassing human performance on the task. Additional tests highlight the importance of accurate image registration to maximize the benefits of the multimodal analysis.

Conclusion: This study advances the field of cytopathology by integrating deep learning methods, multimodal imaging and information fusion to enhance non-invasive early detection of oral cancer. Our approach not only improves diagnostic accuracy, but also allows an efficient, yet uncomplicated, clinical workflow. The developed pipeline has potential applications in other cytological analysis settings. We provide a validated open-source analysis framework and share a unique multimodal oral cancer dataset to support further research and innovation.

1. Introduction

Cancers of the oral cavity and oropharynx are among the most common malignancies in the world. The *GLOBOCAN* database reports that the annual incidence of lip, oral and oropharyngeal cancer in 2022 reached 500,000, and a mortality of 240,000 [11]. Early detection enables timely treatment, thereby substantially improving survival. The average 5-year survival rate in the United States is 69% (2014–2020), but this is highly dependent on when the cancer is found. Only 26% of malignancies are diagnosed while at a local stage, when the 5-year relative survival is as high as 87.5%. Instead, the cancer is often detected late, when it has metastasized, in which case the 5-year survival rate drops to 37.8% [21].

The current medical standard for setting a diagnosis of Oral Cancer (OC) is based on histological examination of a tissue biopsy sample obtained from the suspected tumor site; a time consuming, resource-demanding, and painful procedure. With faster, cheaper, more accessible and non-invasive approaches, early detection, treatment and prognosis of oral and oropharyngeal cancer could be significantly improved [15, 18].

An appealing alternative to histological analysis is *cytological analysis of brush samples* (exfoliative cytology) from the oral cavity of the patients. Brush biopsies can painlessly, and relatively easily [10] be taken during regular visits to a dentist, when suspicious changes in the oral mucosa are observed. The brush samples are then undergoing cytological analysis, commonly performed by a human expert who, using brightfield microscopy (BF), examines Papanicolaou (Pap)-stained cells on a prepared slide. A trained cytologist can detect abnormalities in samples acquired from patients with malignancy, however such visual assessment is both very difficult and very time-consuming. As reported in [40], sensitivity and specificity reached by human experts *on the patient-level diagnosis* are 80% and 86%, respectively, in

*Corresponding author

✉ wenyi.lian.732@student.uu.se (W. Lian);

joakim.lindblad@it.uu.se (J. Lindblad); natasa.sladoje@it.uu.se (N. Sladoje)

ORCID(s): 0009-0000-3069-5366 (W. Lian); 0000-0001-7312-8222 (J. Lindblad); 0000-0002-6041-6310 (N. Sladoje)

liquid-based OC cytology screening (assuming oral high-grade squamous intraepithelial lesion and squamous cell carcinoma as positive). Considering the difficulty to pinpoint very subtle malignant changes in a few, among perhaps 100,000, cells on a glass, there is a great desire for ways to improve the diagnostic accuracy.

Even though an increasing interest in utilizing AI-based decision support for cancer detection in cytology is evident [7, 23, 27], AI-based methods for OC detection are still scarce. Existing results are promising and have confirmed that Deep Neural Networks (DNN) can be trained on Whole Slide Images (WSIs) of Pap-stained cytological samples, to detect OC [24, 29, 44].

A well recognized challenge for the development of AI-based methods in cytology is the severe lack of detailed and reliable annotations. It is not feasible for a cytologist to label each individual cell of a WSI as malignant or healthy, both because of the very large number of cells in each sample (5,000–150,000 cells), and because of the extreme difficulty of the task, where often only very minute differences separate the classes. Therefore, supervised training of DNNs to detect malignancy on the cell level is not realizable. Instead, per-patient labeling is typically used: a label is assigned to the patient's cytological sample, based on histological analysis of a tissue sample acquired at the same location, or (if available) future patient outcome. This type of labeling leads to a weakly supervised learning problem, imposing challenges in training/learning as well as for reliable performance evaluation of developed automated systems.

We aim to increase the amount of information available for automated detection of OC without requiring extensive manual effort invested in per-cell annotations. The latest trends in cancer studies, and life sciences in general, extensively explore the potential of heterogeneous and complementary information about specimens, acquired through diverse imaging (and other) systems and combined in a subsequent correlative analysis of such *multimodal* data. These trends are supported by recent AI-based analysis approaches, which offer efficient multimodal information extraction and fusion [6, 28, 42, 48]. In this study, we evaluate if multimodal cytological image information can be used to improve OC detection.

Multimodal approaches have been explored for OC detection, confirming advantages of combining complementary information from multiple (macroscopic and microscopic) scales [32], or different stainings [35]. However, such approaches typically require advanced sample preparations, which adds to the complexity of imaging. In addition, the correlated analysis most often requires (some type of) multimodal image alignment to establish correspondence between the acquired multimodal data.

To ensure high clinical relevance and applicability of our study, we investigate if an advancement in OC detection can be reached through the correlative analysis of Pap-stained cells from brush biopsies imaged by both BF and fluorescence microscopy (FL) on exactly the same sample,

avoiding any additional staining, and simplifying the required multimodal image alignment. Inspiring studies on fluorescence emitted by Pap-stained samples for improved urothelial cancer detection [39], and for improved detection of inflammation and bacterial infections of respiratory system [17, 26, 43] exist, however no similar study has previously been performed in OC detection.

The main contributions of our work are: (i) We propose an approach based on multimodal imaging of liquid-based cytology (LBC) prepared slides from brush biopsies, combined with AI-based cytological analysis and multimodal information fusion, for improved OC detection; (ii) We propose to combine fluorescence and brightfield WSI, and confirm that this simple and fast multimodal imaging, which requires only one staining, enables OC detection that outperforms approaches based on either of the individual modalities; (iii) We evaluate different deep learning strategies for multimodal information fusion: early, late and intermediate, observing that the intermediate fusion performs best on this task; (iv) We device an efficient multimodal registration pipeline for highly accurate registration of the FL and BF images and confirm, through experimental evaluation, that this is crucial for high OC detection performance; (v) We collect and share a multimodal OC dataset with 766,565 aligned BF and FL image pairs of extracted cells from cytological WSIs: [In_Preparation¹](#); (vi) We contribute to the development of an accurate and reliable, and therefore clinically relevant, AI-based support system for early OC detection.

To facilitate reproducibility, we share our complete implementation and evaluation framework as open source: <https://github.com/MIDA-group/OralCancerMultimodal>.

2. Related Work

Our long-term focus is on the development of an efficient and reliable automated system for early OC detection based on cytological analysis of brush biopsies. In this work, we propose to utilize multimodal image information fusion to increase the informative content extracted from patients' cytological samples by an AI-based cancer detection system. In this section we present previous studies and the existing results that we build on. They cover most relevant aspects of our proposed approach: (i) state-of-the-art in AI-based OC detection by cytological analysis; (ii) experiences of use of multimodal image information in OC detection; (iii) relevance of fluorescence of Pap-stained cells in cancer studies; (iv) state-of-the-art AI-based systems for (biological/biomedical) image information fusion.

AI-supported cytology for OC detection

A survey on AI-methods in cytology [27] from 2019 does not mention any studies on AI-based OC detection among the increasing number of cancer types detected by emerging AI-based approaches. A 2022 survey on AI-approaches for OC detection [1] does not report any methods

¹Will be completed in time for article publication.

applicable to microscopy images of brush biopsies; primary focus is on histological analysis or analysis of photographic images of the oral cavity. A 2021 survey on AI-supported early detection of OC [13] does report on several approaches developed to support exfoliative cytology (including analysis of brush biopsies). Methods mainly rely on shallow machine learning (i.e., manually extracted features, often in combination with Support Vector Machines), and confirm feasibility of AI-based early OC detection from cytological samples, calling for further research and method development. The work presented in [44] evaluates DNNs for the task, and is, as such, a forerunner to our here presented work. This early study does not consider WSIs, but only manually selected regions of cells, and does not include any automated cell detection.

Whole slide imaging is increasingly being used in cytology. A WSI of a cytological slide typically contains tens of thousands of cells. For a sample from a healthy patient, all collected cells are healthy, whereas for a sample from a patient with cancer, some of the cells are malignant (while the majority typically are healthy also in this case). Reliable individual cell-annotation is not feasible, due to the large number of cells and the difficulty of the task. Cytologists, when making a *patient-level* assessment (i.e., assessment of the whole slide, by aggregating information of identified characteristic properties of malignant cells, or absence of such), reach a sensitivity and specificity of the patient diagnosis of around 80% and 86%, respectively [40].

However, the unit of analysis in cytology is the cell and a patient diagnosis is determined based on the presence or absence of malignant cells in a sample. A natural approach in WSI analysis in cytology is, therefore, to extract image patches of a fixed size, each containing a centered in-focus cell nucleus, and to process these by a deep learning classification system. An illustrative example of such extracted cell-patches from a WSI (in two modalities) is shown in Fig. 1. To reach reliable training and validation of such classification models, researchers rely on patient-level annotations, where labels are derived from histological analysis of biopsies, or (if available) from information about future patient outcome. True labels of the individual cells are not known, but are considered to coincide with the label of the sample they belong to. (In other words, the cell label does not indicate malignancy of that cell, but whether the cell originates from a patient with cancer or not.) Consequently, strategies suitable for learning from weak labels, and in particular, Multiple Instance Learning (MIL) approaches [8, 9], are considered. At the same time, the number of malignant cells in a sample is typically much smaller than the total number of cells, which constitutes yet another challenge – MIL on imbalanced training data with very few key instances (malignant cells that determine the diagnosis). Furthermore, while the number of cells in a sample is typically very large, the number of samples (patients) available in studies is often rather low, which is a serious limitation for AI-model development.

Existing studies confirm that an AI-system can be trained on such weakly labeled monomodal cytology data to detect subtle changes in cell morphology caused by malignancy [25, 29]. The CNN-based model proposed in [29] predicts, based on BF data, the patient-level label by aggregating the corresponding cell-instance predictions; it is evaluated in terms of F1-score (harmonic mean of precision and recall), a suitable performance measure for imbalanced data. An alternative, based on Attention-Based MIL (AB-MIL) [20], and modified for efficient use with very large bags is proposed in [3, 25]. A comparative study [24], indicates that the approach proposed in [29] (referred to as Single Instance Learning (SIL) approach) delivers better performance in OC detection than ABMIL with sampling [24, 25], while being less complex and less memory-demanding. It also exhibits better ability to detect key instances, in particular for situations where the ratio of key instances in positive samples is very low (a case which is desired to handle for early cancer detection). Our here presented study therefore builds on the SIL approach as in [29], adjusting it to the multimodal setting.

Multimodal imaging and image analysis for OC detection

Multimodal methods for OC detection are most often developed for tissue analysis (of histological biopsies or in vivo); examples include a combination of macroscopic biochemical imaging of fluorescence lifetime imaging (FLIM) and subcellular morphological imaging of reflectance confocal microscopy (RCM) [30], in vivo assessment by macroscopic white-light imaging of autofluorescence followed by high-resolution microendoscopy of identified regions [46], and widefield fluorescence (WF) imaging with non-linear optical microscopy (Multi-Photon and Second Harmonic Generation) [32].

Studies that confirm an increase of informative content in oral brush biopsies from sequential staining of the samples include an early example presented in [35], where Pap, Feulgen, and Silver nitrate staining were combined in (manually performed) correlative analysis. This study, which does not rely on any specialized integrated multimodal imaging system, is relevant for our use-case since it confirms an information gain from multimodal imaging; however we aim to avoid re-staining of the samples as well as to automate the process of extraction and fusion of information.

Fluorescence microscopy of Pap-stained cytological slides

The studies [2, 39] show that FL imaging of Pap-stained urothelial cells reveals information which is relevant for the detection of early neoplastic lesions. The distributions of fluorescence for tumoral urothelial cells and normal cells appear rather different (the former being characterized by a perimembrane fluorescence localization, and the latter exhibiting an intracellular fluorescence). These results, relying on the analysis of photophysical properties of the different dyes used for the Pap staining, encourage utilization of FL

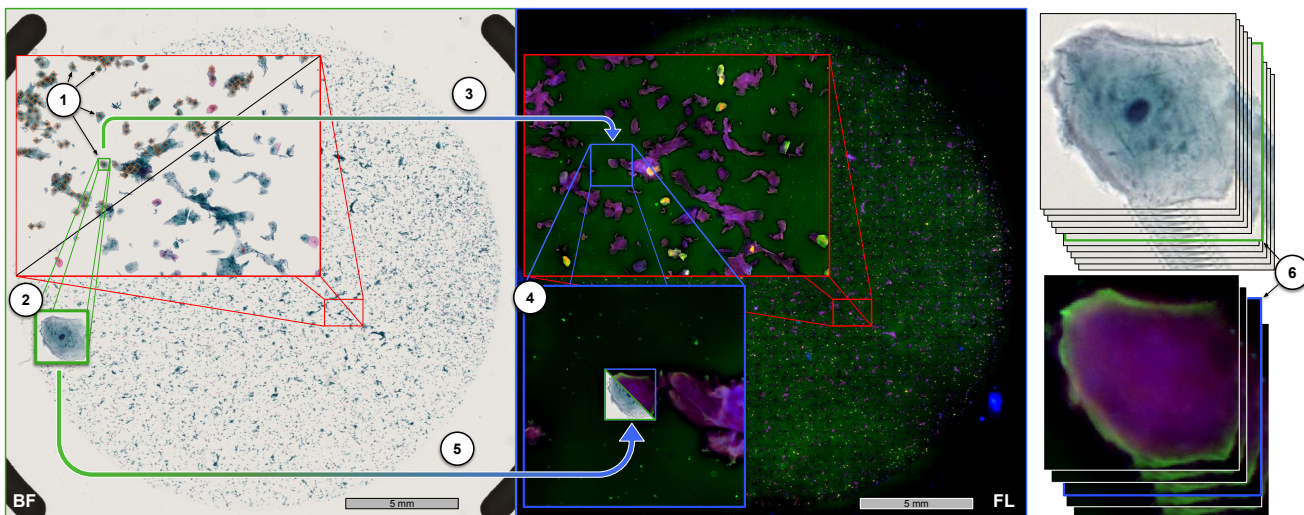


Figure 1: Illustration of the aligned patch extraction procedure, starting from a rigidly aligned pair of BF and FL WSIs. 1. Nucleus detection in BF (orange lozenges; 31,336 detected in this slide); 2. Patch extraction 256x256 px in BF (green square); 3. Rigid mapping of nucleus position into FL image; 4. Large 768x768 px patch extraction (larger blue square); 5. Translation only CMIF-based registration for pixel perfect 256x256 px patch extraction in FL image; 6. Selection of best the focus level in BF (11 levels) and FL (5 levels). Only three out of the four FL channels (emission wavelengths 668,517,465) are visualized (as RGB).

imaging, while changing neither the sampling of the specimens nor the Pap-staining protocol. Further analysis [14], provided some insight in the underlying biological phenomena behind the peri-membrane fluorescence.

Several other studies have explored the advantages of FL of Pap-stained samples in contexts different from cancer detection. For detection of mycobacterial species in lymph node fine-needle aspiration specimens [45], it is observed that the fluorescence information, complementary to the standard brightfield microscopy, improves specificity of the analysis, with a minimal additional investment. Other related results include cytological diagnosis of *Pneumocystis carinii* in bronchoalveolar lavage specimens [43], detection of *Aspergillus* infections [17], detection of oral *Candida* [41] and the diagnosis of *Mycobacterium kansasii* tuberculosis [26], all indicating informative content of the (auto-)fluorescence of Pap-stained samples.

Inspired by these results, we acquire both BF and FL images of Pap-stained LBC oral cytological slides. We aim to enable AI-based multimodal information extraction and integration, towards improved early OC detection.

AI-based multimodal information fusion

Integration of complementary information from diverse data sources allows more reliable cancer diagnosis. However, to perform manual/visual correlative analysis across diverse data modalities becomes a very complex task, calling for support by AI-based information fusion and analysis methods [6, 28]. Different strategies are considered in a variety of studies [34, 48]. *Early fusion* utilizes one model to process the combined information from all modalities. The combined input can be created by, e.g., concatenation of the input vectors, or their element-wise sums or products. *Late fusion*, on the other hand, integrates information from

different modalities at the final decision level, after a separate model is trained for each modality. The aggregation of the models' predictions can be performed by e.g., averaging, majority voting, or through a learned model.

To allow a gradual influence of the multimodal information on the extraction of features from individual modalities, a number of strategies for *intermediate fusion* have been suggested. The different methods exploit the multimodal information in different ways, allowing the intermediate integrated content (features) to backpropagate and influence, to a higher or lower extent, the overall process and its output. Relevant examples include [5, 16, 22].

In our here presented study we evaluate early, late, and intermediate multimodal information fusion strategies, to reach improved OC detection from BF and FL Pap-stained microscopy images.

3. Multimodal Oral Cancer Dataset

For the purpose of this study we create a multimodal OC dataset consisting of accurately aligned BF and FL images ($n=766,565$) of Pap-stained in-focus cells acquired from healthy individuals and patients with histologically confirmed OC. The procedure employed to create the dataset is illustrated in Fig. 1 and described in detail below.

Sample acquisition

We collected LBC prepared Pap-stained slides of brush-sampled cells from the oral cavity of 19 adult patients. Positive samples ($n=8$) were obtained from the anatomical location of histopathologically verified oral squamous cell carcinoma lesions. Out of the negative samples ($n=11$), two were diagnosed as healthy based on histopathological analysis, whereas the majority of negative samples ($n=9$)

were acquired from healthy adults without an accompanying histological analysis due to the invasive nature of the associated tissue biopsy.

Samples were collected (Folktandvården, Dept. of Oro-facial Medicine, Södersjukhuset, Region Stockholm, Sweden) with a Cytobrush Plus GT (Medscand Medical, Cooper Surgical company, USA) for cytological assessment. The brush was rubbed against the oral mucosa for approximately 30 s and then immediately placed in a vial of Preserv-Cyt™ transport medium (Hologic, Inc. USA), spun around the walls of the vial for approximately 10 s and then removed. Collected specimens were processed according to the standard procedure at the Department of Pathology and Cytology, previously described in [10]. LBC slides were prepared using a ThinPrep TP5000 processor (Hologic, Inc., Bedford, MA, USA) and stained using a Gemini AS slide Stainer (Thermo Scientific, Gothenburg, Sweden) according to regressive Papanicolaou (Pap) staining technique [38].

BF and FL microscopy imaging

We first image the Pap-stained slides under white light using a NanoZoomer S60 digital slide scanner (Clinical Pathology and Cytology, Uppsala University Hospital), 40 \times , 0.75 NA objective, at 11 z-offsets (stepping 0.4 μ m) providing RGB BF WSIs of approximately 100,000 \times 100,000 pixels, 0.23 μ m/pixel.

We subsequently acquire FL images of the same Pap-stained slides using a Zeiss Axio Scan Z1 slide scanner (BioVis platform of Uppsala University), 20 \times , 0.8 NA, at 5 z-offsets (stepping 1.0 μ m), excitation wavelengths: {353, 493, 553, 653}, emission filter wavelengths: {465, 517, 568, 668}, providing 4-channel FL WSIs of approximately 77,000 \times 77,000 pixels, 0.33 μ m/pixel.

Correction for spatial intensity nonuniformity

For the FL images, we correct for spatial intensity nonuniformity by, for each channel separately, subtracting a low-pass Gaussian filtered version of the image ($\sigma = 10\%$ of image side length) followed by a linear rescaling of the intensities to the range [0, 1], with a saturation of bright pixels which surpass 4 times the 99th percentile.

Nucleus detection and focus selection in BF

We employ a modified version of the method described in Lu *et al.* [29] to detect cell nuclei in each of the BF WSIs. First, images are downsampled by a factor 4 \times 4. A small (8 convolution layers) regression U-Net [36] is trained based on manually marked nucleus locations (each modeled with a small 2D Gaussian kernel, $\sigma = 3$ px) in three slides. (These three slides are not later used in the study.) For each slide, nuclei locations are detected at local maxima of height > 0.5 in the prediction output. To not miss nuclei in the top or bottom focus-layers, the nucleus detection is run on images from z-offsets $\{-2, 0, 2\}$ μ m; a detection is registered if found in any of the three z-levels. Example output from the nucleus detection step can be seen in Step 1 of Fig. 1.

For each detected nucleus location, 256 \times 256 pixel regions are cut out from each z-level at the full image

resolution (Step 2 of Fig. 1), and the z-level which provides the best focus is selected (BF part of Step 6 of Fig. 1). We perform focus selection by using a center weighted (knowing that the nucleus is in the center of the cut out patch) modified Laplacian (LAP2) [31, 33]. The method is evaluated on a separate test set consisting of BF images of 100 nuclei, each acquired at 11 focus levels. The “ground truth” is created by asking 8 experts to select the best focus level for each nucleus and taking the median of the 8 assigned labels as true best focus. The proposed method reaches an accuracy of 93% on this data set; outperforming both the method presented in [29] and the average human expert, the two reaching 84% and 85.5% accuracy, respectively, on the same data.

Aligned patch extraction from FL data

To register the FL and BF images, we use the *glob-align*, global multimodal image registration method proposed in [49]. This method is based on fast computation of cross-mutual information in the frequency domain. It is shown to reach state-of-the-art performance on a range of modality combinations, including biomedical data.

For each pair of FL and BF WSIs, we first estimate a global translation and rotation on a 32 \times downsampled version, incorporating the known spatial scale factor of 1.472 between the different modalities. Due to small drift during the scanning and accumulated stitching errors, this slide-level alignment does not reach pixel-level accuracy. We therefore perform a translation-only re-alignment for each individual nucleus. Knowing the global rigid transformation, we compute, for each detected nucleus in the BF image, its corresponding location in the FL image and there extract, at the middle z-level, a 768 \times 768 pixel region at the full image resolution (Steps 3 and 4 of Fig. 1). For each extracted region we (again) run *globalign* (with known scale and rotation) to find the best match with the corresponding middle z-level patch of the BF image at pixel-level accuracy (Step 5 of Fig. 1). We then extract the corresponding 256 \times 256 pixel region from the considered FL patch at the level which provides the best focus, similar as for the BF data (FL part of Step 6 of Fig. 1).

The contrast in the FL images is sometimes very low, which makes the registration unreliable. To ensure high quality data, we remove the 5% cells with the lowest FL contrast (based on the used focus measure), as well as cells for which the fine-level registration does not agree with the alignment of neighboring cells (such “failed registration” most often coincide with low image contrast).

Labeling

The cells are labeled according to the patient-level labels: all cells from the samples originating from patients with a detected malignancy are labeled as “positive”, whereas all cells from the samples associated with healthy patients are labeled as “negative”. Note that this labeling does not assign cell-level labels to indicate malignancy, since a majority of cells from patients with malignancy are actually healthy, and only a subset is indeed malignant.

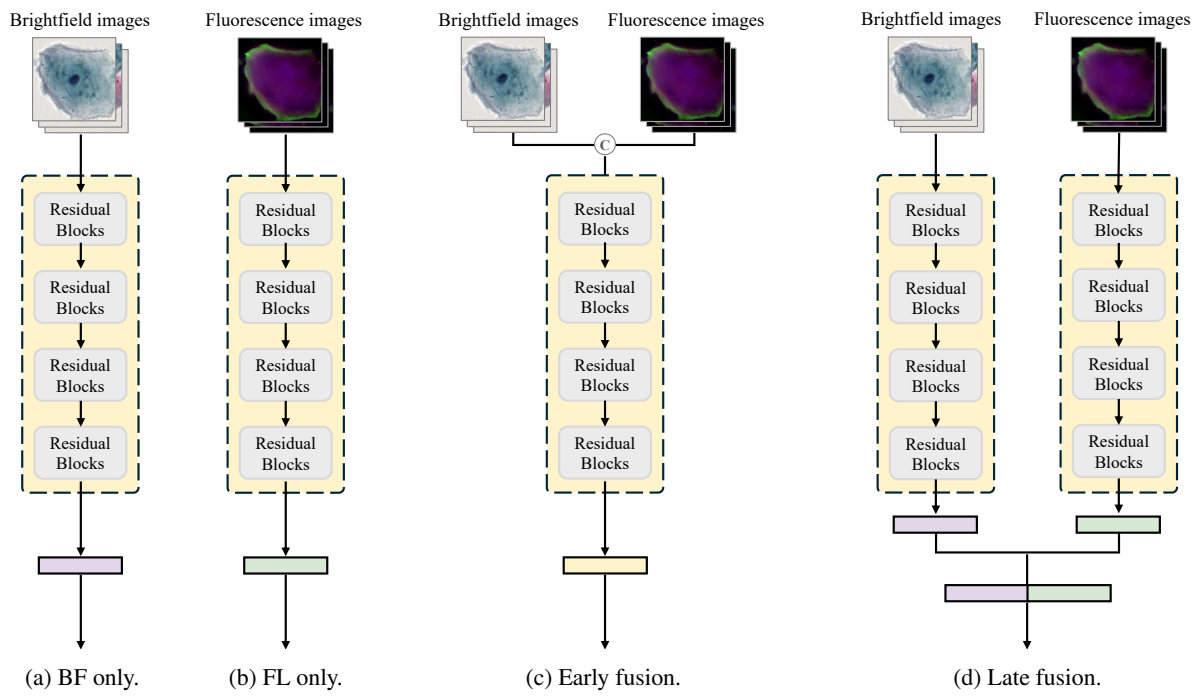


Figure 2: Classification of microscopy images based on (a) and (b) single-modality; (c) early fusion; (d) late fusion frameworks.

Complete dataset

The above described procedure provides us with in total 766,565 cut-outs, each with an in-focus cell in the center, well aligned in the two modalities; 599,167 patches are from 11 healthy and 167,398 are from 8 OC patients. We make this collected and accurately aligned multimodal OC dataset available for research purposes: [In_Preparation²](#).

4. OC Classification Methods

The power of multimodal approaches lies in complementarity of the combined modalities, such that their integrated informative content exceeds the information available from each individual modality alone. We explore several multimodal fusion strategies and architectures, adjusted to extract and integrate information from BF and FL images of Pap-stained cells, to provide an information-rich content for AI-based OC detection. In the following subsections we introduce the main general fusion strategies, overview three recent advanced intermediate multimodal fusion networks – Multimodal Transfer Module (MMTM) [22], Hyper-connected Convolutional Neural Network (HcCNN) [5], and Co-Attention Fusion Network (CAFNet) [16], and finally summarize the modifications made to adjust these methods for OC detection from our dataset.

4.1. Multimodal fusion frameworks

A main challenge in deep learning-based multimodal fusion is how to effectively fuse the different modalities to best use the advantages of the complementary information they bring in, enhancing feature extraction or final representation

learning, while still not disrupting the learning process [4]. Depending on the location of the fusion process in the workflow, the information integration methods are generally categorized into early, late, and intermediate fusion [34].

Early fusion directly merges data sources at the initial processing stage. As depicted in Fig. 2c, images from different modalities are merged before being input into the network. This approach allows the exploitation of cross-correlations between different modalities at the pixel level. However, this requires the data to be accurately aligned to reach a unified representation suitable for further joint processing.

Late fusion, as illustrated in Fig. 2d, typically involves concatenating high-level features, independently extracted by different (suitably selected) networks from each modality, to perform the final prediction of class labels. Late fusion is expected to be more robust than early fusion, since the integration of the high-level features alleviates the need of accurate image alignment. However, due to fusing features only in the final layer, this type of architecture has a much weaker ability to establish, and utilize, correspondence between the different modalities.

Intermediate fusion utilizes features from different levels of the decision model to enhance the model's ability to capture complex data relationships and to improve accuracy compared to late or early fusion. Whereas early fusion methods typically processes data in one branch, and late fusion methods comprise two branches (one for each modality), intermediate fusion frameworks often feature an additional (intermediate) “fusion branch”, to process multi-level fused

²Will be completed in time for article publication.

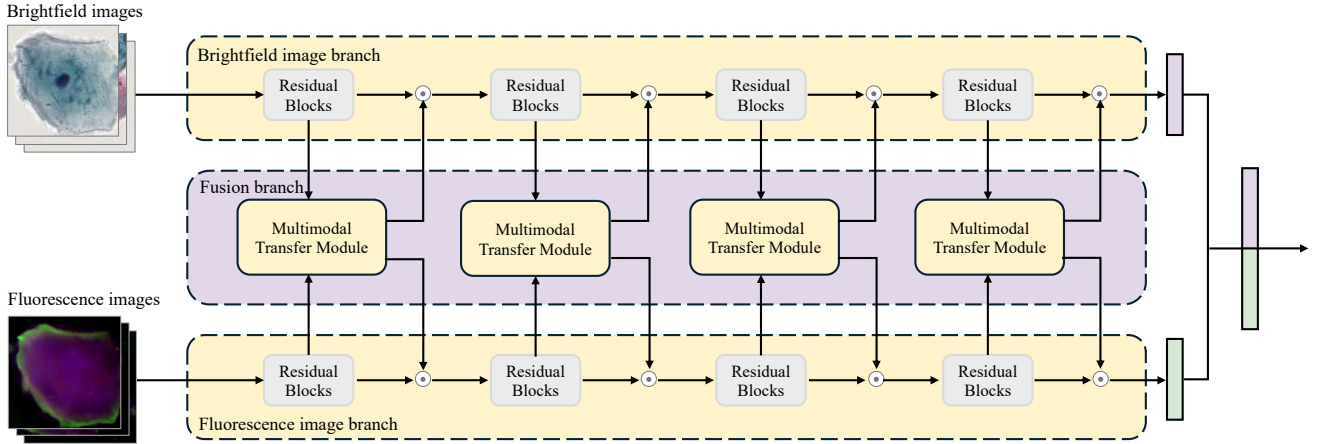


Figure 3: Overview of the Multimodal Transfer Module (MMTM) framework, adapted from [22].

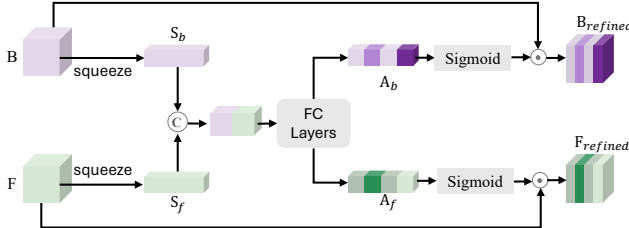


Figure 4: Details of the multimodal transfer module (MMTM) block, adapted from [22].

information in the network. Several approaches have been proposed regarding how to utilize the fusion branch within the network architecture, with the aim to find a most beneficial balance between monomodal feature enhancement and cross-modal information fusion. We evaluate three state-of-the-art deep fusion models, being representative examples of different strategies for intermediate fusion, to find a best performing one for the task of multimodal OC detection.

4.1.1. MMTM

Multimodal Transfer Module (MMTM) architecture [22] is equipped with a fusion branch, in which a sequence of MMTM blocks inputs features from the two single-modality branches and, for each block, outputs two weight maps which are multiplied with the original (single-modality) features. The framework is illustrated in Fig. 3. The fusion branch does not directly contribute to the final representation. Instead, it is only used to enhance each of the monomodal feature maps in their separate layers. MMTM extends the *squeeze* and *excitation* (SE) module [19] to produce weight maps for the channels, as a specific channel attention mechanism. This modified channel attention also receives two sets of single modality features to accommodate multimodal scenarios.

The detailed structure of the MMTM block is shown in Fig. 4. Feature maps B and F are extracted from each of the monomodal inputs. A “squeeze” operation compresses the global information within the input feature maps using

Global Average Pooling (GAP), resulting in the squeezed features S_b and S_f which are concatenated into a combined multimodal vector. The concatenated vector is passed through two fully connected layers to generate two modulation weight maps (A_b and A_f) for the different modalities. The two weight maps are normalized using sigmoid function and used to recalibrate the single-modality branches through a multiplication with the original feature maps in the channel dimension. The MMTM block adapts well across various spatial dimensions and can be easily integrated with existing network structures. However, it has a limited ability to capture interactions between the modalities and primarily adjusts, rather than fully fuses, the features.

4.1.2. HcCNN

The fusion branch in the Hyper-connected Convolutional Neural Network (HcCNN) [5] receives monomodal features from two single-modality branches but, as opposed to the MMTM network, does not use them to affect the original single-modality branches. Instead, the fused features are directly incorporated as a part of the final representations used for prediction. An overview of HcCNN is depicted in Fig. 5. The Hyper-Connected Module (HC module) is used at several levels to perform multimodal feature extraction and fusion. Each HC module comprises a fusion block, a residual block, and a multi-scale attention (MsA) block, to merge and refine information extracted from the different modalities.

The fusion block concatenates, as input, single-modality features B and F , and a fused feature map U' from the previous HC-module. It outputs a fused feature map, which is further processed by several residual blocks, resulting in an enhanced feature set U_f . Subsequently, the MsA block, illustrated in Fig. 6, is used to refine the complementary information with multi-scale attention. The output U of the MsA block is a spatial weight map, multiplied with the original fused feature U_f .

The channel-wise attention used in HcCNN to fuse single-modality features adjusts the importance of channels

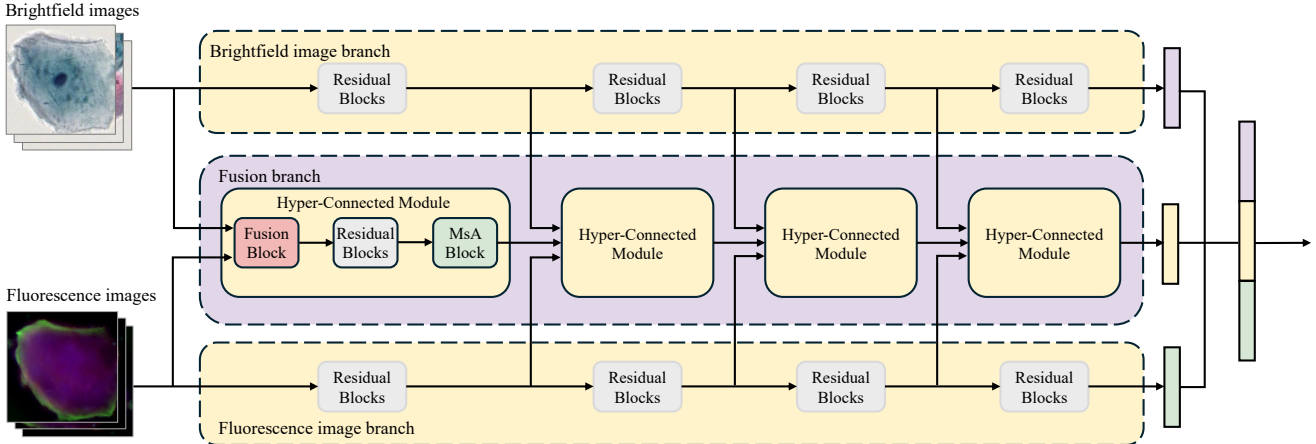


Figure 5: Overview of the hyper-connected convolutional neural network (HcCNN), adapted from [5].

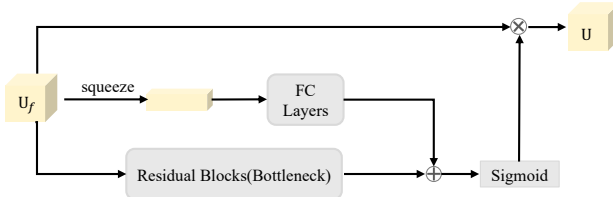


Figure 6: Details of the HcCNN multi-scale attention block (MsA Block), adapted from [5].

based on global information within each channel, but is not able to fully utilize cross-modal interactions.

4.1.3. CAFNet

Co-Attention Fusion Network (CAFNet) [16] draws inspiration from both MMTM and HcCNN. Its fusion branch not only enhances the feature learning of single-modality branches, but also integrates information from different modalities as the fused output. By employing a cross-attention mechanism, CAFNet may capture spatial interrelations of the modalities. Fig. 7 provides an overview of the CAFNet architecture. The fusion branch comprises four CAF modules, each containing a cross-attention (CA) block and an attention fusion (AF) block. The CA block has dual-modality input and output, and employs a cross-attention mechanism to enhance feature representation learning.

Fig. 8 illustrates the details of the cross-attention mechanism, which enables the model to capture spatial relationships and dependencies between the corresponding regions of the image pairs. Three metrics are learned for each modality: “key” and “query” are used to generate weight maps, which are multiplied with the “value” metrics of the other modality to support multimodal interaction and improve the feature learning.

The AF block, illustrated in Fig. 9, introduces a pixel-wise attention mechanism to dynamically tune weight ratios for multimodal feature fusion. It takes as input refined features B_{refined} and F_{refined} from the CA block, fuses them

(pixel-wise attention) into U_{bf} , and then (by the same mechanism), fuses U_{bf} with U'_{fusion} from the previous stage, to obtain the final feature map U_{fusion} .

Finally, the output of the fusion branch is concatenated with the two single-modality feature vectors for the label prediction.

The cross-attention mechanism in CAFNet allows exploiting the interaction between modalities, but increases model complexity, making this model computationally heavy and its training at a higher risk of overfitting.

4.2. Task-specific multimodal model adjustments

Our aim is to evaluate if multimodal information fusion of BF and FL image data can contribute to improve OC detection from cytological WSI, compared to what is achieved based on either of the two modalities (BF and FL) alone. We therefore compare performances of monomodal, as well as several multimodal approaches (described above) on our created BF & FL multimodal OC dataset.

For a meaningful and fair method comparison, we implement suitable modifications across all the considered fusion methods. In particular, the original versions of the HcCNN [5] and CAFNet [16] methods employ loss functions designed for the multi-label classification tasks targeted in the original publications. HcCNN uses a single loss function to evaluate features concatenated from three branches against ground truth labels. In contrast, the original CAFNet is based on a more intricate (and computationally costly) loss function architecture, with each of the three branches subjected to an individual loss function, supplemented by an additional overall loss function for the concatenated output from all branches, resulting in four collaborative loss functions within its framework. As for MMTM [22], it is originally proposed for tasks unrelated to biomedical applications, with no details provided for the loss functions in the original publication. To better accommodate our single-label binary classification task and the use of mixup data augmentation, we adjust the considered intermediate fusion

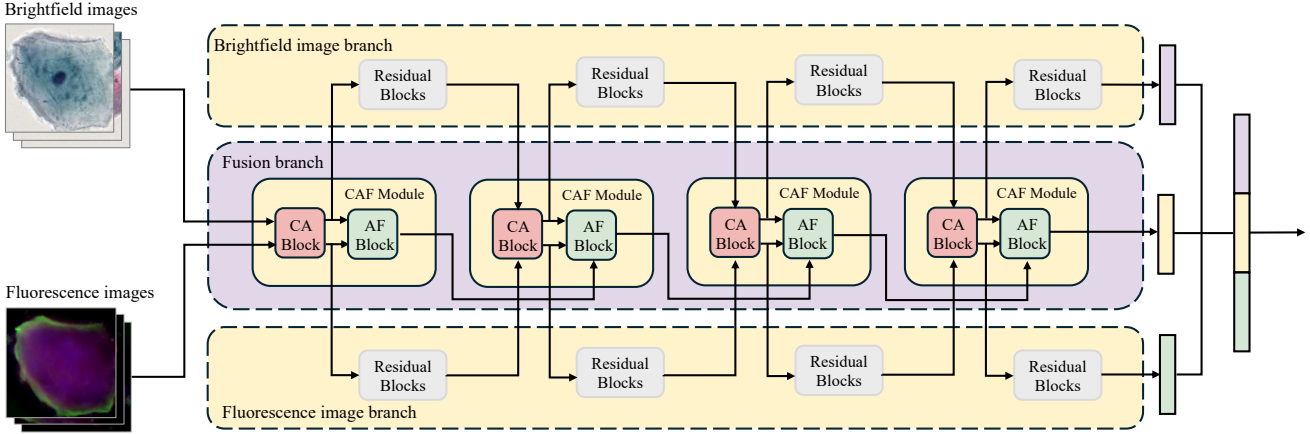


Figure 7: Overview of the Co-Attention Fusion Network (CAFNet) framework, adapted from [16].

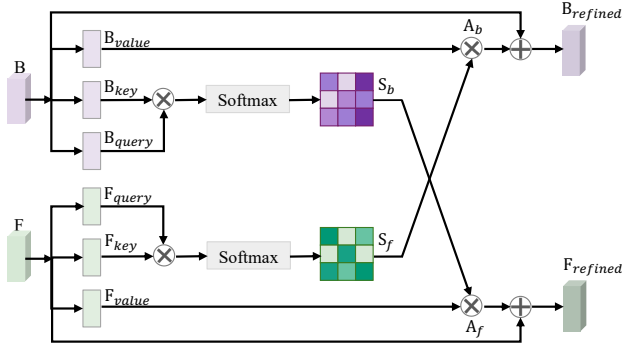


Figure 8: Details of the Co-Attention (CA) block in CAFNet, adapted from [16].

methods by utilizing the same mixup-based binary classification loss on the final prediction for all the approaches evaluated in this study.

To fit our OC dataset, we slightly modify the input convolution of all approaches with the correct channel count for each modality, i.e., 3 channels for BF image input and 4 channels for FL image input. For early fusion, we concatenate the channels into a multimodal image with 7 channels, which are processed by a single-branch network.

We use ImageNet [37] pretrained ResNet-50 as the backbone for all networks, except the first and last layers which are trained from scratch (randomly initialized). The multi-branch networks use the same architecture for each branch, but learn different parameters.

5. Experimental Setup

5.1. Data partitioning

We utilize a variation of 3-fold cross-validation (CV) to efficiently exploit our limited data. To prevent data leakage, we partition the dataset into four subsets with individual patients. Each partition contains two patients diagnosed with oral cancer and two or three healthy (i.e., non-oral cancer)

individuals. Table 1 provides a summary of the dataset partitioning, detailing the numbers of images and patients from cancer/healthy groups across the four partitions. Within each partition, the cancer and non-cancer ratios are nearly identical, with the proportion of cancer images consistently around 22% in all partitions, reflecting the overall distribution.

We designate partition 0 as a validation set for choosing suitable hyperparameters, while the remaining three partitions are utilized in a rotating manner for testing and training in each fold. To not waste useful training data, our evaluation is divided into two distinct phases. In the “Initial Validation” phase, we first tune hyperparameters using partition 0 as a common validation set for each fold. Following this, we move into the “Full Training” phase, rejoining partition 0 into the training set and retrain the network (using the tuned set of hyperparameters) for the final evaluation on the (for the given fold) strictly separated test set.

5.2. Data augmentation

BF and FL provide distinct imaging modalities with major differences in image appearance and characteristics. For efficient learning, it is essential to implement modality-specific data augmentation strategies. For the BF images, we apply the following data augmentation steps: either (probability $p = 0.4$) posterization to 3-bit color depth, or ($p = 0.2$) Gaussian blurring (kernel size 5 and sigma 1.5), or ($p = 0.4$) solarization, inverting pixel values above a threshold of 100. Subsequent color jittering changes brightness by up to 0.5, and contrast, saturation, and hue by up to 0.2 each. Following the jittering, we normalize BF images based on the mean and variance of all BF images in the dataset (this step does not require access to any labels). For FL images, we individually apply color jittering to each channel (brightness and contrast at 0.8), along with Gaussian blurring (kernel size 5, sigma in the range 0.3 to 3.2). These images are then normalized using the mean and variance from all FL images. Finally, geometric transforms, such as random flipping and resizing are jointly applied to both BF and FL images, ensuring the preservation of the spatial alignment of the two modalities during the data augmentation step. Specifically,

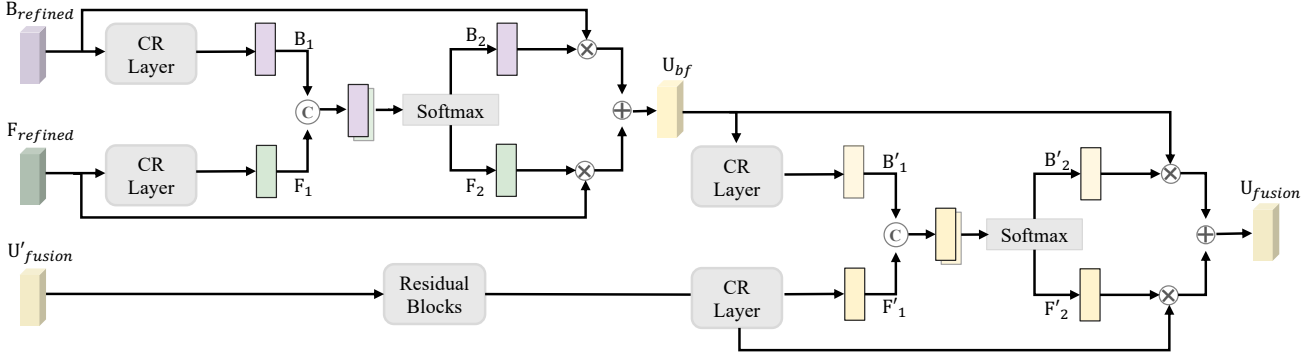


Figure 9: Details of the attention fusion block (AF Block), adapted from [16]. “CR Layer” stands for Channel Reduction, which uses three consecutive convolutions to produce a 1-channel feature map (e.g., B_1 , F_1 , B'_1 , F'_1). Corresponding 1-channel features are concatenated to form fusion feature maps, which are then processed through a softmax function to generate weight maps for pixel-wise attention fusion.

Table 1: Summary of the OC dataset: number of patches and patients, for each class and each partition.

Partition	Cancer patches (patients)	Healthy patches (patients)	Total patches (patients)
0	40,764 (2)	149,796 (3)	190,560 (5)
1	39,605 (2)	144,914 (3)	184,519 (5)
2	42,523 (2)	147,769 (2)	190,292 (4)
3	44,506 (2)	156,688 (3)	201,194 (5)
Sum	167,398 (8)	599,167 (11)	766,565 (19)

we resize (bilinear interpolation) the 256×256 images to a uniform size of 224×224 to fit a joint standard size of the architectures. Mixup data augmentation is then used to create mixed (joint BF and FL) inputs by linearly combining each sample with another randomly chosen sample from the same batch [47], using $\alpha = 0.8$. For validation and testing, we exclusively apply the same normalization and resizing as in training (i.e., no test-time augmentation).

5.3. Training details

The total number of training epochs is set to 30, selected based on performance stability on the validation set (observed for all the models), with the last epoch used for final evaluation. The batch size is set to 256 for all methods, except CAFNet for which we use a batch size of 128 due to its higher memory requirements. We adopt the AdamW optimizer with an initial learning rate 8×10^{-5} . The weight decay is set to 0.1. The *CosineAnnealing* learning rate scheduler is used, with minimum learning rate set to 1×10^{-7} and T_max set to the number of training epochs, which is 30 in our case. We use a mixup-based binary cross-entropy (BCE) loss with class weights. Specifically, for each training batch, samples enhanced with the mixup technique are given by

$$x_{\text{mix}} = \lambda \cdot x_a + (1 - \lambda) \cdot x_b, \quad (1)$$

where $\lambda \sim \text{Beta}(\alpha, \alpha)$ is a coefficient that controls the mixing proportion of the original data x_a and the perturbed data x_b .

The model’s output logits are defined as $\hat{y} = p_{\theta}(x_{\text{mix}})$, where θ is the network parameter, then the mixup-based BCE loss is

$$\mathcal{L} = \lambda \cdot \text{BCE}(\hat{y}, y_a, w_a) + (1 - \lambda) \cdot \text{BCE}(\hat{y}, y_b, w_b), \quad (2)$$

where y_a and y_b denote the labels corresponding to x_a and x_b , respectively. The weights w_a and w_b are used to adjust imbalanced classes, with a value of 0.22 for non-cancer cases and 0.78 for cancer cases, both are computed from the training dataset.

All hyperparameters mentioned above are selected based on observed performance during the “Initial Validation” phase. Each parameter is evaluated across a range of values. The final choice is determined by the highest average F1 score achieved. All methods are implemented using the PyTorch framework and trained on a single NVIDIA A100 Tensor Core GPU with 80GB memory.

5.4. Comparison and evaluation metrics

The compared methods are divided into three categories: (i) single-modality networks; (ii) simple multimodal methods (i.e., early and late fusion); and (iii) intermediate fusion methods (MMTM [22], HcCNN [5], and CAFNet [16]). We compare their performance utilizing the following metrics: F1 score, accuracy, Receiver Operating Characteristic Area Under the Curve (ROC AUC), recall, and precision. We also present the full confusion matrix for a comprehensive results’ view. Due to the imbalanced nature of our OC dataset, we select F1 score as the primary evaluation metric, while also reporting other metrics for completeness.

6. Results and Analysis

6.1. Brightfield vs. Fluorescence

We first compare the performance of single-modality methods (i.e., BF-only and FL-only). As summarized in Table 2 (and also Table 3), the FL-only method outperforms the BF-only method w.r.t. all considered metrics, in particular showing 4.55 percentage points of improvement in terms of

Table 2: Average F1 score, Accuracy, ROC AUC, Recall, and Precision under 3-fold cross-validation on the OC dataset, comparing data augmentation with and without color jitter for the monomodal BF and FL image-only methods.

Method	F1 score	Accuracy	ROC AUC	Recall	Precision
BF-only	0.6944	0.8521	0.8958	0.7265	0.6894
BF-only w/o color jitter	0.6776	0.8482	0.8779	0.7529	0.6563
FL-only	0.7399	0.8768	0.9039	0.7736	0.7246
FL-only w/o color jitter	0.5514	0.7336	0.7404	0.6481	0.5196

the average F1 score (under 3-fold cross-validation). Consistently, Table 4 reports higher counts of True Negatives (TN) and True Positives (TP) for the FL method.

We perform an ablation study regarding the used pre-processing steps and observe that the color jittering is the most important, particularly for the FL image augmentation. Table 2 presents the performance of BF-only and FL-only methods, with and without color jitter in the data augmentation processes. The methods utilizing the complete data augmentation strategy consistently outperform those where color jitter is omitted. We therefore conduct all further experiments utilizing the complete augmentation.

6.2. Monomodal vs. Multimodal

We conduct an overall comparison between multimodal approaches and single-modality techniques. The results, presented in Table 3, show that multimodal methods consistently outperform single-modality methods over all metrics. (This trend is confirmed over all folds, as presented in Table A.1-A.5 in the Appendix.) For example, early fusion reaches an average F1 score improvement of over 8 percentage points compared to the best-performing single-modality method, FL-only. The same trend extends to accuracy, ROC AUC, precision and recall, where multimodal approaches also excel. Table 4 provides further evidence, showing higher counts of TN and TP, and greater accuracy rates for multimodal methods. Fig. 10 visually confirms the consistent superiority of multimodal approaches throughout the training process. This continuous and consistent advantage underscores the inherent benefits of utilizing multiple modalities.

6.3. Early and Late vs. Intermediate fusion

As can be seen in Table 3, early fusion outperforms late fusion in all observed metrics. Early fusion reaches a 1.69 percentage points higher average F1 score and 0.89 percentage points higher average accuracy than late fusion. Observing Fig. 10 it is clear that early fusion surpasses late fusion in overall performance across our key metrics also throughout the training.

Focusing on the more sophisticated intermediate fusion techniques, we observe in Table 3 and Fig. 10 that MMTM exhibits slightly lower F1 score, accuracy, and ROC AUC compared to the early fusion method. HcCNN exceeds MMTM in all metrics and surpasses late and early fusion in accuracy. CAFNet emerges as the overall leading method, reaching an F1 score of 83.34% and the top accuracy and

ROC AUC, as can be seen in Table 3. Table 4 reveals that MMTM records the highest number of TN and early fusion captures the most TP, while CAFNet effectively balances the number of TN and TP.

6.4. Additional experiments

Impact of misalignment. We explore the impact of misalignment of (the multimodal) input images on the multimodal fusion performance, with a specific focus on early, late, and CAFNet methods. To introduce alignment discrepancies to multimodal inputs, we manually shift the BF modality images by $d \in \{0, 2, 4, 8, 16\}$ pixels, while the FL images are kept at their original position. The results are presented in Fig. 11. We observe that the performances of early fusion and CAFNet degrade across both metrics as the misalignment is introduced. As expected, late fusion appears the most robust w.r.t. variations in alignment, and is the method which reaches the highest F1 score for the more severely misaligned data. CAFNet, which works best when images are well aligned, experiences a substantial drop in performance if the multimodal images are misaligned. The pixel-wise cross-modal attention of the method appears to give a clear performance boost on well aligned data, however this boost breaks down once faced with misaligned data. A general observation is that accurate alignment of the multimodal data appears to be crucial for reaching top performance.

Attentions in multimodal fusion. He *et al.* [16] attribute the state-of-the-art performance of CAFNet to the integration of the CA (Channel Attention) and AF (Attention Fusion) blocks. To quantify the individual contributions of these components, we modify the CAFNet architecture with two variants: CAFNet without CA block and CAFNet without AF block. As presented in Table 5, omitting either the AF block or the CA block decreases the performance over all metrics. Removing the CA block leads to the larger drop in performance, indicating that cross-attention appears to play an important role in the multimodal information fusion.

Two-stream monomodal methods. When comparing the performance of a multimodal model and a monomodal model, it is relevant to ascertain that the two models have similar complexity [12]. We therefore include a performance comparison between a two-stream setup used in the monomodal case (inputting the same modality into both streams) and a two-stream network which processes two modalities. Table 6 shows that utilizing two-stream networks for BF and FL modalities slightly outperform their single-stream counterparts. However, these monomodal models still stay far behind the multimodal approaches. For example, the late fusion of similar complexity, with a clear margin provides higher scores across all metrics, highlighting the power of multimodal information fusion.

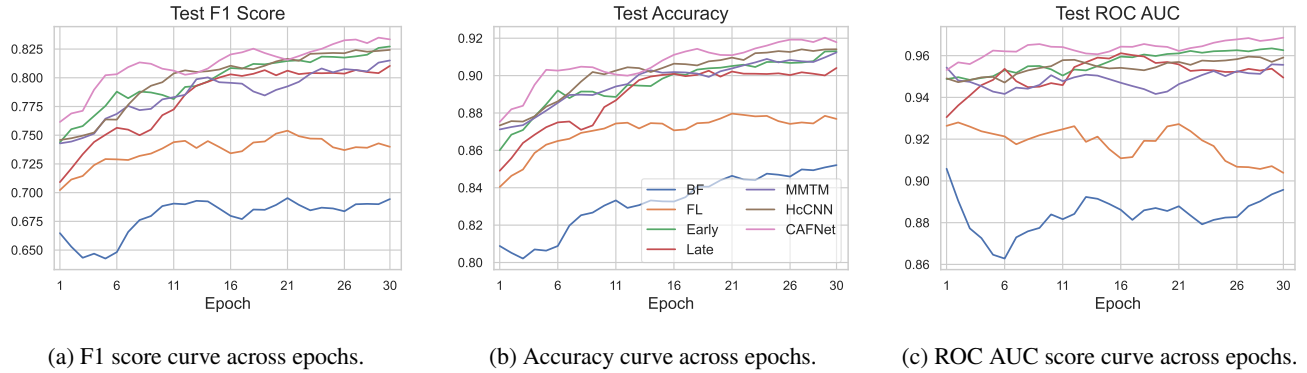


Figure 10: Test set performance metrics for the considered monomodal and multimodal classification methods on the OC dataset, averaged over 3-fold cross-validation, for each epoch during (the final) training. The legend is consistent for all three plots.

Table 3: Performance of the considered methods under 3-fold cross-validation: Average **F1 score**, **Accuracy**, **ROC AUC**, **Recall**, and **Precision** (with standard deviations). Higher scores indicate better performance. The highest averages are highlighted in bold.

Method	F1 score \pm std	Accuracy \pm std	ROC AUC \pm std	Recall \pm std	Precision \pm std
BF-only	0.6944 \pm 0.1267	0.8521 \pm 0.0735	0.8958 \pm 0.0660	0.7265 \pm 0.0539	0.6894 \pm 0.2443
FL-only	0.7399 \pm 0.0817	0.8768 \pm 0.0494	0.9039 \pm 0.0507	0.7736 \pm 0.0208	0.7246 \pm 0.1750
Early	0.8273 \pm 0.0959	0.9130 \pm 0.0525	0.9626 \pm 0.0397	0.9192 \pm 0.0665	0.7619 \pm 0.1551
Late	0.8104 \pm 0.1005	0.9041 \pm 0.0585	0.9495 \pm 0.0337	0.8893 \pm 0.0267	0.7593 \pm 0.1845
MMTM	0.8151 \pm 0.0760	0.9124 \pm 0.0425	0.9556 \pm 0.0245	0.8541 \pm 0.0692	0.7978 \pm 0.1749
HcCNN	0.8243 \pm 0.1006	0.9141 \pm 0.0546	0.9591 \pm 0.0346	0.8797 \pm 0.0410	0.7887 \pm 0.1820
CAFNet	0.8334 \pm 0.0954	0.9179 \pm 0.0529	0.9686 \pm 0.0351	0.8994 \pm 0.0756	0.7934 \pm 0.1819

Table 4: The overall results of the **confusion matrix** for each method, showing the numbers of True Negatives (TN), False Positives (FP), False Negatives (FN), and True Positives (TP). The highest values for TN and TP are highlighted in bold, corresponding to the lowest values for FP and FN, respectively.

Method	TN↑	FP↓	FN↓	TP↑
BF-only	398,684	50,687	34,887	91,747
FL-only	407,268	42,103	28,759	97,875
Early	409,638	39,733	9,932	116,702
Late	408,422	40,949	13,940	112,694
MMTM	416,293	33,078	15,086	111,548
HcCNN	415,338	34,033	15,060	111,574
CAFNet	415,040	34,331	12,483	114,151

7. Discussion

Our above reported classification results are obtained on the cell/patch level. Considering our overarching goal of improved early OC detection, these results should be aggregated, to provide predictions on the patient level. A simple aggregation strategy is to determine the ratio of the predicted malignant (positive) and healthy (negative) cells for each patient, and to perform dichotomisation of the patients to the two classes based on, e.g., a suitably determined threshold.

In Fig. 12 we present the relative numbers of cells predicted as positive, by the BF-only, FL-only, and CAFNet models. A patient-level decision should be reached taking into consideration more information, but a simple observation of ratios does allow some observations. By placing the threshold for a positive/negative patient-level classification at 60% of positive cells, we obtain, by using CAFNet model, classification of patients with 0 FN and 1 FP (with the corresponding F1 score: 0.92; accuracy: 0.93; recall: 1.0; precision: 0.86). However, even if these results are highly promising, the so far acquired dataset (19 patients, out of which 5 are excluded in this evaluation to prevent data leakage) is too small for any reliable conclusions to be yet drawn at the patient level. We are continuously acquiring more (multimodal) data, and based on the results of this study, we expect that FM imaging will be a part of our future pipeline.

Considering the general challenge of multimodal image alignment, of our particular interest was evaluating the effect of misaligned multimodal input on the performance of the different information fusion models/strategies. Our observations support the often reported findings that the alignment of the input data has a strong impact on performance of the early fusion strategies. However, we also observe a similar effect in case of the intermediate fusion approach. It is reasonable to assume that, in case of CAFNet – the best performing approach on the aligned data, the sophisticated

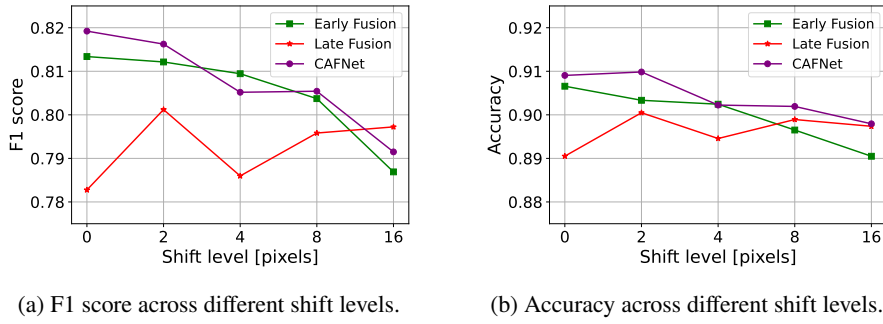


Figure 11: Performance metrics for early fusion, late fusion and CAFNet methods at increasing levels of displacement between the two modalities (emulating a less accurate image registration).

Table 5: Performance of CAFNet and its variants (CAFNet without the CA block and CAFNet without the AF block) on the OC dataset in terms of F1 score, accuracy, ROC AUC score, recall and precision.

Method	F1 score	Accuracy	ROC AUC	Recall	Precision
CAFNet	0.8334	0.9179	0.9686	0.8994	0.7934
CAFNet without AF block	0.8252	0.9143	0.9608	0.8844	0.7881
CAFNet without CA block	0.7910	0.8921	0.9448	0.8813	0.7304

Table 6: Average F1 score, accuracy, ROC AUC, recall, and precision under 3-fold cross validation on the OC dataset, comparing single-stream and two-stream networks for BF and FL modalities.

Method	F1 score	Accuracy	ROC AUC	Recall	Precision
BF-only	0.6944	0.8521	0.8958	0.7265	0.6894
two-stream BF-only	0.7015	0.8492	0.9005	0.7612	0.6764
FL-only	0.7399	0.8768	0.9039	0.7736	0.7246
two-stream FL-only	0.7451	0.8792	0.9048	0.7838	0.7213
Late fusion	0.8104	0.9041	0.9495	0.8893	0.7593

pixel-wise attention mechanisms responsible for its excellent performance on the aligned data, are also a main reason for a high sensitivity of the model to misalignment in the multimodal input.

The attention mechanisms and the extra fusion branch added to the intermediate model architectures substantially increase memory and computational demands, which may limit their use in resource-constrained environments. Our experiments show that early fusion, requiring only about one-third of the training time of CAFNet achieves comparable results and can be a recommended approach to balance the advantages of multimodal information with the required resources for its processing.

8. Conclusion

In this study, we present a workflow for the early detection of oral cancer from cytology WSIs, exploiting the information gain reached by a multimodal approach. We create a multimodal OC dataset, imaged with BF and FL microscopy, and perfectly aligned on the patch/cell level. We evaluate

various deep learning strategies for fusing multimodal information from the created dataset. Our findings demonstrate that multimodal methods consistently outperform single-modality approaches across all evaluated metrics. Among the methods investigated, CAFNet – an intermediate fusion approach – stands out as the most effective, achieving an F1 score of 83.34% and an accuracy of 91.79% for the cell-level classification.

Acknowledgements

This work is supported by: Sweden’s Innovation Agency (VINNOVA), grants 2017-02447, 2020-03611, and 2021-01420, the Swedish Research Council, grants 2017-04385 and 2022-03580, and Cancerfonden projects 22 2353 Pj and 22 2357 Pj. A part of the computations was enabled by resources provided by the National Academic Infrastructure for Supercomputing in Sweden (NAIIS) and the Swedish National Infrastructure for Computing (SNIC) at Chalmers Centre for Computational Science and Engineering (C3SE), partially funded by the Swedish Research Council through grants 2022-06725 and 2018-05973. We are grateful to M. Matić for accurate cell location annotations.

Additional information

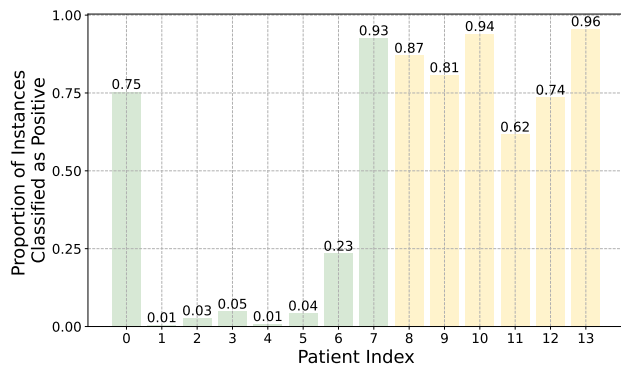
The study was performed in compliance with the Declaration of Helsinki and approved by the Ethical Review Board Stockholm Sweden (2015-1213-31 and 2019-00349). Informed written consent was obtained from all participants. The study does not involve minors.

Competing interests

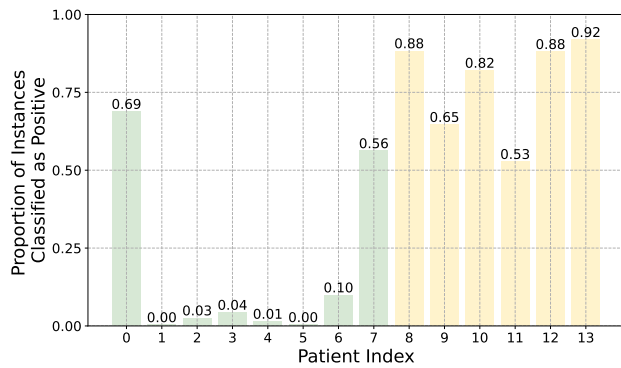
The authors declare no competing interests.

References

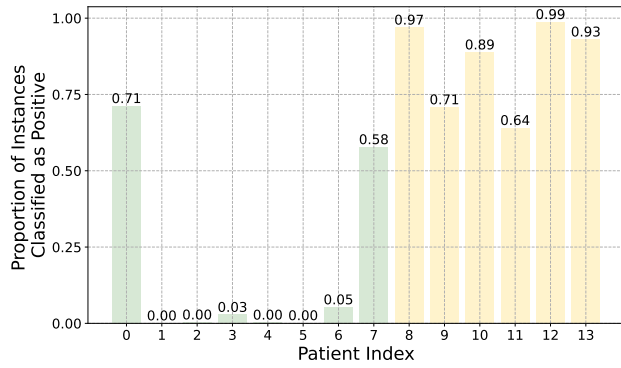
- [1] Al-Rawi, N., Sultan, A., Rajai, B., Shuaeeb, H., Alnajjar, M., Alketbi, M., Mohammad, Y., Shetty, S.R., Mashrah, M.A., 2022. The effectiveness of artificial intelligence in detection of oral cancer. International Dental Journal 72, 436–447. doi:10.1016/j.identj.2022.03.001.
- [2] Alsibai, K.D., Daste, G., Ferlicot, S., Fabre, M., Steenkeste, K., Salleron, J., Hammoudi, Y., Fontaine-Aupart, M.P., Eschwegehe, P., 2020. Fluorescence emitted by Papanicolaou-stained urothelial cells improves sensitivity of urinary conventional cytology for detection



(a) BF-only.



(b) FL-only.



(c) CAFNet.

Figure 12: The relative numbers of cells predicted as positive for each patient in the oral cancer dataset, using different methods. Instances with a sigmoid score > 0.5 are classified as positive, indicating the presence of oral cancer. Patients 0–7 (green) are negative, and the rest (yellow) are positive.

of urothelial tumors. *World Journal of Oncology* 11, 204–215. doi:10.14740/wjon1305.

[3] Andersson, A., Koriakina, N., Sladoje, N., Lindblad, J., 2022. End-to-end multiple instance learning with gradient accumulation, in: IEEE International Conference on Big Data (Big Data), IEEE. pp. 2742–2746. doi:10.1109/BigData55660.2022.10020801.

[4] Baltrušaitis, T., Ahuja, C., Morency, L.P., 2018. Multimodal machine learning: A survey and taxonomy. *IEEE Transactions on Pattern Analysis and Machine Intelligence* 41, 423–443. doi:10.1109/TPAMI.2018.2798607.

[5] Bi, L., Feng, D.D., Fulham, M., Kim, J., 2020. Multi-label classification of multi-modality skin lesion via hyper-connected convolutional neural network. *Pattern Recognition* 107, 107502. doi:10.1016/j.

patcog.2020.107502.

[6] Boehm, K.M., Khosravi, P., Vanguri, R., Gao, J., Shah, S.P., 2022. Harnessing multimodal data integration to advance precision oncology. *Nature Reviews Cancer* 22, 114–126. doi:10.1038/s41568-021-00408-3.

[7] C., K., Vimala, H., J., S., 2024. A systematic review of artificial intelligence techniques for oral cancer detection. *Healthcare Analytics* 5, 100304. doi:10.1016/j.health.2024.100304.

[8] Carboneau, M.A., Cheplygina, V., Granger, E., Gagnon, G., 2018. Multiple instance learning: A survey of problem characteristics and applications. *Pattern Recognition* 77, 329–353. doi:10.1016/j.patcog.2017.10.009.

[9] Cheplygina, V., de Bruijne, M., Pluim, J., 2019. Not-so-supervised: A survey of semi-supervised, multi-instance, and transfer learning in medical image analysis. *Medical Image Analysis* 54, 280–296. doi:10.1016/j.media.2019.03.009.

[10] Edman, K., Stark, C.R., Basic, V., Lindblad, J., Hirsch, J.M., 2023. Dental hygienists and dentists as providers of brush biopsies for oral mucosa screening. *International Journal of Dental Hygiene* 21, 524–532. doi:10.1111/idh.12713.

[11] Ferlay, J., Ervik, M., Lam, F., et al., 2024. Global cancer observatory: Cancer today (version 1.1). URL: <https://gco.iarc.who.int/today>. Lyon, France: International Agency for Research on Cancer. Online; accessed 4 June 2024.

[12] Garcia, N.C., Morerio, P., Murino, V., 2019. Learning with privileged information via adversarial discriminative modality distillation. *IEEE Transactions on Pattern Analysis and Machine Intelligence* 42, 2581–2593. doi:10.1109/TPAMI.2019.2929038.

[13] García-Pola, M., Pons-Fuster, E., Suárez-Fernández, C., Seoane-Romero, J., Romero-Méndez, A., López-Jornet, P., 2021. Role of artificial intelligence in the early diagnosis of oral cancer. A scoping review. *Cancers (Basel)* 13, 4600. doi:10.3390/cancers13184600.

[14] Gutierrez, C., Pinson, X., Jarnouen, K., Charpentier, M., Pineau, R., Lallement, L., Pedeux, R., 2022. Characterization of the peri-membrane fluorescence phenomenon allowing the detection of urothelial tumor cells in urine. *Cancers* 14. doi:10.3390/cancers14092171.

[15] Haj-Hosseini, N., Lindblad, J., Hasséus, B., Kumar, V.V., Subramaniam, N., Hirsch, J.M., 2024. Early detection of oral potentially malignant disorders: a review on prospective screening methods with regard to global challenges. *Journal of Maxillofacial and Oral Surgery* 23, 23–32. doi:10.1007/s12663-022-01710-9.

[16] He, X., Wang, Y., Zhao, S., Chen, X., 2023. Co-attention fusion network for multimodal skin cancer diagnosis. *Pattern Recognition* 133, 108990. doi:10.1016/j.patcog.2022.108990.

[17] Hettlich, C., Küpper, T., Wehle, K., Pfitzer, P., 1998. Aspergillus in the Papanicolaou stain: morphology, fluorescence and diagnostic feasibility. *Cytopathology* 9, 381–388. doi:10.1046/j.1365-2303.1998.00123.x.

[18] Hirsch, J.M., Sandy, R., Hasséus, B., Lindblad, J., 2023. A paradigm shift in the prevention and diagnosis of oral squamous cell carcinoma. *Journal of Oral Pathology & Medicine* 52, 826–833. doi:10.1111/jop.13484.

[19] Hu, J., Shen, L., Sun, G., 2018. Squeeze-and-excitation networks, in: Proceedings of the IEEE conference on computer vision and pattern recognition, pp. 7132–7141. doi:10.1109/TPAMI.2019.2913372.

[20] Ilse, M., Tomczak, J., Welling, M., 2018. Attention-based deep multiple instance learning, in: International conference on machine learning, PMLR. pp. 2127–2136. doi:10.48550/arXiv.1802.04712.

[21] Institute, N.C., 2024. Surveillance, epidemiology, and end results (seer) program. URL: <https://seer.cancer.gov>. online; accessed 4 June 2024.

[22] Joze, H.R.V., Shaban, A., Iuzzolino, M.L., Koishida, K., 2020. MMTM: Multimodal transfer module for CNN fusion, in: Proceedings of the IEEE/CVF Conference on Computer Vision and Pattern Recognition (CVPR), pp. 13289–13299. doi:10.1109/CVPR42600.2020.01330.

[23] Kim, D., Sundling, K.E., Virk, R., et al., 2024. Digital cytology part 2: artificial intelligence in cytology: a concept paper with review and recommendations from the American Society of Cytopathology Digital Cytology Task Force. *Journal of the American Society of Cytopathology* 13, 97–110. doi:10.1016/j.jasc.2023.11.005.

[24] Koriakina, N., Sladoje, N., Bašić, V., Lindblad, J., 2024. Deep multiple instance learning versus conventional deep single instance learning for interpretable oral cancer detection. *PLOS ONE* 19, 1–23. doi:10.1371/journal.pone.0302169.

[25] Koriakina, N., Sladoje, N., Lindblad, J., 2021. The effect of within-bag sampling on end-to-end multiple instance learning, in: International Symposium on Image and Signal Processing and Analysis (ISPA), IEEE. pp. 183–188. doi:10.1109/ISPA52656.2021.9552170.

[26] Küpper, T., Wehle, K., Marzahn, S., Pfizer, P., 1995. The cytologic diagnosis of mycobacterium kansasi tuberculosis by fluorescence microscopy of Papanicolaou-stained specimens. *Cytopathology* 6, 331–338. doi:10.1111/j.1365-2303.1995.tb00579.x.

[27] Landau, M.S., Pantanowitz, L., 2019. Artificial intelligence in cytopathology: a review of the literature and overview of commercial landscape. *Journal of the American Society of Cytopathology* 8, 230–241. doi:10.1016/j.jasc.2019.03.003.

[28] Lipkova, J., Chen, R.J., Chen, B., Lu, M.Y., Barbieri, M., Shao, D., Vaidya, A.J., Chen, C., Zhuang, L., Williamson, D.F., Shaban, M., Chen, T.Y., Mahmood, F., 2022. Artificial intelligence for multimodal data integration in oncology. *Cancer Cell* 40, 1095–1110. doi:10.1016/j.ccr.2022.09.012.

[29] Lu, J., Sladoje, N., Stark, C.R., Ramqvist, E.D., Hirsch, J.M., Lindblad, J., 2020. A deep learning based pipeline for efficient oral cancer screening on whole slide images, in: International Conference on Image Analysis and Recognition, Springer. pp. 249–261. doi:10.1007/978-3-030-50516-5_22.

[30] Malik, B.H., Jabbour, J.M., Cheng, S., Cuenca, R., Cheng, Y.S.L., Wright, J.M., Jo, J.A., Maitland, K.C., 2016. A novel multimodal optical imaging system for early detection of oral cancer. *Oral and Maxillofacial Pathology* 121, 290–300. doi:10.1016/j.oooo.2015.10.020.

[31] Nayar, S.K., Nakagawa, Y., 1994. Shape from focus. *IEEE Transactions on Pattern Analysis and Machine Intelligence* 16, 824–831. doi:10.1109/34.308479.

[32] Pal, R., Villarreal, P., Yu, X., Qiu, S., Vargas, G., 2020. Multimodal widefield fluorescence imaging with nonlinear optical microscopy workflow for noninvasive oral epithelial neoplasia detection: a pre-clinical study. *Journal of Biomedical Optics* 25, 116008. doi:10.1117/1.JBO.25.11.116008.

[33] Pertuz, S., Puig, D., Garcia, M.A., 2013. Analysis of focus measure operators for shape-from-focus. *Pattern Recognition* 46, 1415–1432.

[34] Ramachandram, D., Taylor, G.W., 2017. Deep multimodal learning: A survey on recent advances and trends. *IEEE Signal Processing Magazine* 34, 96–108. doi:10.1109/MSP.2017.2738401.

[35] Remmerbach, T.W., Meyer-Ebrecht, D., Würflinger, T., Bell, A.A., Schneider, T.E., Nietzke, N., Böcking, B.F.A., 2009. Toward a multimodal cell analysis of brush biopsies for the early detection of oral cancer. *Cancer Cytopathology* 117, 228–235. doi:10.1002/cnc.20028.

[36] Ronneberger, O., Fischer, P., Brox, T., 2015. U-Net: Convolutional networks for biomedical image segmentation, in: Proceedings of Medical Image Computing and Computer-Assisted Intervention – MICCAI, Springer. pp. 234–241. doi:10.1007/978-3-319-24574-4_28.

[37] Russakovsky, O., et al., 2015. ImageNet large scale visual recognition challenge. *International Journal of Computer Vision* 115, 211–252. doi:10.1007/s11263-015-0816-y.

[38] Soost, H., Falter, E., Otto, K., 1979. Comparison of two Papanicolaou staining procedures for automated prescreening. *Analytical and Quantitative Cytology* 1, 37–42.

[39] Steenkiste, K., Lécart, S., Deniset, A., Pernot, P., Eschwège, P., Ferlicot, S., Lévéque-Fort, S., Briandet, R., Fontaine-Aupart, M.P., 2007. Ex vivo fluorescence imaging of normal and malignant urothelial cells to enhance early diagnosis. *Photochemistry and Photobiology* 83, 1157–1166. doi:10.1111/j.1751-1097.2007.00079.x.

[40] Sukegawa, S., et al., 2020. Clinical study on primary screening of oral cancer and precancerous lesions by oral cytology. *Diagnostic Pathology* 15, 1–6. doi:10.1186/s13000-020-01027-6.

[41] Titinchi, F., Du Toit, J., Hille, J.J., Neethling, G., 2011. The diagnostic accuracy of autofluorescence microscopy of pap smears for oral candidal hyphae. *International Journal of Oral & Maxillofacial Pathology* 2, 28–34.

[42] Vollmer, A., Hartmann, S., Vollmer, M., Shavlokhova, V., Brands, R.C., Kübler, A., Wollborn, J., Hassel, F., Couillard-Despres, S., Lang, G., Saravi, B., 2024. Multimodal artificial intelligence-based pathogenomics improves survival prediction in oral squamous cell carcinoma. *Scientific Reports* 14. doi:10.1038/s41598-024-56172-5.

[43] Wehle, K., Blanke, M., Koenig, G., Pfizer, P., 1991. The cytological diagnosis of pneumocystis carinii by fluorescence microscopy of Papanicolaou stained bronchoalveolar lavage specimens. *Cytopathology* 2, 113–120. doi:10.1111/j.1365-2303.1991.tb00395.x.

[44] Wieslander, H., Forslid, G., Bengtsson, E., Wählby, C., Hirsch, J.M., Runow Stark, C., Kecheril Sadanandan, S., 2017. Deep convolutional neural networks for detecting cellular changes due to malignancy, in: Proceedings of the IEEE International Conference on Computer Vision Workshops, pp. 82–89. doi:10.1109/ICCVW.2017.18.

[45] Wright, C.A., van Zyl, Y., Burgess, S.M., Blumberg, L., Leiman, G., 2004. Mycobacterial autofluorescence in Papanicolaou-stained lymph node aspirates: A glimmer in the dark? *Diagnostic Cytopathology* 30, 257–260. doi:10.1002/dc.20009.

[46] Yang, E.C., Vohra, I.S., Badaoui, H., Schwarz, R.A., Cherry, K.D., Quang, T., Jacob, J., Lang, A., Bass, N., Rodriguez, J., Williams, M.D., Vigneswaran, N., Gillenwater, A.M., Richards-Kortum, R.R., 2019. Development of an integrated multimodal optical imaging system with real-time image analysis for the evaluation of oral premalignant lesions. *Journal of Biomedical Optics* 24, 1–10. doi:10.1117/1.JBO.24.2.025003.

[47] Zhang, H., Cisse, M., Dauphin, Y.N., Lopez-Paz, D., 2018. mixup: Beyond empirical risk minimization, in: International Conference on Learning Representations. doi:10.48550/arXiv.1710.09412.

[48] Zitnik, M., Nguyen, F., Wang, B., Leskovec, J., Goldenberg, A., Hoffman, M.M., 2019. Machine learning for integrating data in biology and medicine: Principles, practice, and opportunities. *Information Fusion* 50, 71–91. doi:10.1016/j.inffus.2018.09.012.

[49] Överstedt, J., Lindblad, J., Sladoje, N., 2022. Fast computation of mutual information in the frequency domain with applications to global multimodal image alignment. *Pattern Recognition Letters* 159, 196–203. doi:10.1016/j.patrec.2022.05.022.

A. Appendix

Table A.1: Reached **F1 scores** for the considered methods under 3-fold cross-validation on the multimodal OC dataset, showcasing each method's performance across three independent folds and their average scores. Higher score indicates better performance, with the highest scores highlighted in bold.

Method	Fold 1	Fold 2	Fold 3	Average
BF-only	0.6494	0.8375	0.5963	0.6944
FL-only	0.6752	0.8318	0.7128	0.7399
Early	0.7223	0.9104	0.8492	0.8273
Late	0.7091	0.9101	0.8120	0.8104
MMTM	0.7311	0.8792	0.8350	0.8151
HcCNN	0.7184	0.9185	0.8359	0.8243
CAFNet	0.7263	0.9090	0.8650	0.8334

Table A.2: Reached **accuracy** for the considered methods under 3-fold cross-validation on the multimodal OC dataset, showcasing each method's performance across three independent folds and their average accuracy. Higher accuracy indicates better performance, with the highest scores highlighted in bold.

Method	Fold 1	Fold 2	Fold 3	Average
BF-only	0.8204	0.9362	0.7998	0.8521
FL-only	0.8354	0.9315	0.8636	0.8768
Early	0.8567	0.9606	0.9219	0.9130
Late	0.8446	0.9617	0.9059	0.9041
MMTM	0.8670	0.9514	0.9188	0.9124
HcCNN	0.8569	0.9658	0.9195	0.9141
CAFNet	0.8594	0.9623	0.9320	0.9179

Table A.3: Reached **ROC AUC scores** for the considered methods under 3-fold cross-validation on the multimodal OC dataset, showcasing each method's performance across three independent folds and their average scores. Higher score indicates better performance, with the highest scores highlighted in bold.

Method	Fold 1	Fold 2	Fold 3	Average
BF-only	0.8824	0.9674	0.8374	0.8958
FL-only	0.8938	0.9589	0.8590	0.9039
Early	0.9168	0.9855	0.9856	0.9626
Late	0.9153	0.9827	0.9504	0.9495
MMTM	0.9287	0.9767	0.9614	0.9556
HcCNN	0.9210	0.9885	0.9678	0.9591
CAFNet	0.9282	0.9917	0.9860	0.9686

Table A.4: Reached **recall** for the considered methods under 3-fold cross-validation on the multimodal OC dataset, showcasing each method's performance across three independent folds and their average recall. Higher recall indicates better performance, with the highest scores highlighted in bold.

Method	Fold 1	Fold 2	Fold 3	Average
BF-only	0.7750	0.7360	0.6685	0.7265
FL-only	0.7972	0.7582	0.7652	0.7736
Early	0.8684	0.8949	0.9944	0.9192
Late	0.8821	0.8669	0.9189	0.8893
MMTM	0.8424	0.7914	0.9284	0.8541
HcCNN	0.8502	0.8621	0.9266	0.8797
CAFNet	0.8691	0.8436	0.9854	0.8994

Table A.5: Reached **precision** for the considered methods under 3-fold cross-validation on the multimodal OC dataset, showcasing each method's performance across three independent folds and their average precision. Higher precision indicates better performance, with the highest scores highlighted in bold.

Method	Fold 1	Fold 2	Fold 3	Average
BF-only	0.5588	0.9713	0.5382	0.6894
FL-only	0.5856	0.9211	0.6671	0.7246
Early	0.6183	0.9264	0.7409	0.7619
Late	0.5928	0.9577	0.7274	0.7593
MMTM	0.6457	0.9889	0.7586	0.7978
HcCNN	0.6220	0.9828	0.7613	0.7887
CAFNet	0.6238	0.9855	0.7708	0.7934